Available online at https://link.springer.com/journal/42241
http://www.jhydrodynamics.com
Journal of Hydrodynamics, 2023, 35(2): 199-209
https://doi.org/10.1007/s42241-023-0026-y

Wall-modeled large eddy simulation for the flows around an axisymmetric body of revolution

Song-tao Chen[1], Lu-chun Yang[2], Wei-wen Zhao[1], De-cheng Wan[1*]
1. *Computational Marine Hydrodynamics Lab (CMHL), School of Naval Architecture, Ocean and Civil Engineering, Shanghai Jiao Tong University, Shanghai 200240, China*
2. *Wuhan Second Ship Design and Research Institute, Wuhan 430205, China*

(Received May 5, 2023, Revised May 10, 2023, Accepted May 11, 2023, Published online May 25, 2023)
©China Ship Scientific Research Center 2023

Abstract: The flow around an axisymmetric body of revolution (DARPA SUBOFF bare model) at $Re = 1.2 \times 10^7$ is numerically investigated using the wall-modeled large eddy simulation (WMLES). To evaluate the capabilities of WMLES in such wall-bounded turbulent flows, the effects of the wall stress model and sampling distance are systematically studied. The numerical results of the non-equilibrium wall stress model with an appropriate sampling distance are in good agreement with the experiments in terms of pressure coefficient, skin-friction coefficient, and drag coefficient. On this basis, the thickening of the turbulent boundary layer and the expansion of the wake can be clearly observed through flow visualization, especially using the Liutex vortex identification method.

Key words: Wall-modeled large eddy simulation (WMLES), axisymmetric body of revolution, wall stress model, sampling distance, Liutex, SUBOFF

0. Introduction

The complex flows around underwater vehicles have always been a research hotspot in marine hydrodynamics, which is strongly correlated with the generation and propagation of underwater noise. Compared with blunt bodies, underwater vehicles are usually streamlined bodies. Among them, the DARPA SUBOFF model with and without appendages are the most popular benchmark models and have accumulated extensive experimental data[1-3]. At the same time, with the development of high-performance computers, computational fluid dynamics (CFD) has become another powerful tool for predicting and analyzing the hydrodynamic characteristics. On this basis, many scholars have carried out numerical simulations on the flow around the SUBOFF model. The Reynolds-averaged Navier-Stokes (RANS) method is capable of predicting global quantities[4] such as hydrodynamic forces but fails to capture the unsteady flow characteristics. In this regard, the detached eddy simulation (DES) method has been adopted to resolve the flow field in the wake[5-6], while the boundary layer region is still modeled by the RANS approach.

However, the solution strategy for the boundary layer has a strong influence on such wall-bounded turbulent flows. Therefore, the large eddy simulation (LES) method is considered to be the most suitable approach to capture the flow characteristics. Posa and Balaras[7] carried out wall-resolved LES (WRLES) on the DARPA SUBOFF model with appendages at $Re = 1.2 \times 10^6$. To capture all essential flow features, a cylindrical structured mesh consisting of 2.9×10^9 nodes was adopted in their simulation. Kumar and Mahesh[8] numerically investigated the flow over the DARPA SUBOFF bare model at $Re = 1.1 \times 10^6$ using WRLES. The near-wall flow structures were captured using an unstructured body-fitted mesh of 6.08×10^9 cells. As we can see, WRLES requires a fairly high mesh resolution in high Reynolds number turbulent flows, where most of the mesh (> 90%) is used to resolve the inner part of the boundary layer[9]. To reduce computational cost, the wall-modeled LES (WMLES)[9-11] is proposed. Compared with WRLES, WMLES only resolves the large eddies in the outer layer while modeling the effect of small eddies in the viscous inner layer. Recently, WMLES has been successfully applied to the numerical simulation of

Project supported by the National Natural Science Foundation of China (Grant No. 52131102), the National Key Research and Development Program of China (Grant Nos. 2022YFC2806705, 2019YFB1704200).
Biography: Song-tao Chen (1997-), Male, Ph. D.,
E-mail: songtao.chen@sjtu.edu.cn
Corresponding author: De-cheng Wan,
E-mail: dcwan@sjtu.edu.cn

axisymmetric bodies. Posa and Balaras[12] combined the immersed-boundary (IB) method with WMLES and simulated the flow around the DARPA SUBOFF model with appendages at $Re=1.2\times10^7$. In their simulations, the wall modelling strategy was only active in the middle parallel region based on their previous study[7]. When the Reynolds number was increased by an order of magnitude, the numerical results agreed well with the experiments without a significant increase in the computational mesh. Shi et al.[13] implemented WMLES in the framework of the diffusive-interface IB method and simulated the DARPA SUBOFF bare model at $Re=1.2\times10^6$. They investigated the effects of the wall stress model and sampling point. On this basis, Zhou et al.[14] numerically studied the turbulent flow around the fully appended SUBOFF model at $Re=1.2\times10^7$, focusing on noise prediction. In their simulations, the non-equilibrium wall stress model was used for WMLES. Zhou et al.[15] compared the numerical results of WRLES and WMLES for the turbulent flow around an axisymmetric body of revolution at $Re=1.9\times10^6$. The results of both approaches agree well with the experimental data in terms of velocity statistics and pressure fluctuations.

In the present study, the flow around an axisymmetric body of revolution (DARPA SUBOFF bare model) at $Re=1.2\times10^7$ is numerically investigated using the wall-modeled LES. The primary objectives are to (1) Study the effects of the wall stress model and sampling distance, (2) Analyze the flow field using the Liutex method. The remainder of this paper is organized as follows. First, the numerical methods are introduced in detail, including governing equations, wall stress models, and vortex identification methods. Then, the numerical setup is mainly described from the mesh configuration and numerical schemes. Next, the effects of the wall stress model and sampling distance on the pressure coefficient, skin-friction coefficient, and drag coefficient are systematically studied. After that, the turbulent flow filed near the hull and in the wake is visualized and analyzed. Finally, the main conclusions are drawn.

1. Numerical methods

1.1 *Governing equations*

The open-source CFD platform OpenFOAM is used to carry out all numerical simulations. In the present study, the filtered incompressible Navier-Stokes equations are used, including the continuity and momentum equations:

$$\nabla\cdot\tilde{\boldsymbol{u}}=0 \tag{1}$$

$$\frac{\partial\tilde{\boldsymbol{u}}}{\partial t}+\nabla\cdot(\tilde{\boldsymbol{u}}\tilde{\boldsymbol{u}})=-\frac{\nabla\tilde{p}}{\rho}+\nu\nabla^2\tilde{\boldsymbol{u}}-\nabla\cdot\boldsymbol{\tau}^{\mathrm{sgs}} \tag{2}$$

where $\tilde{\boldsymbol{u}}$ is the filtered velocity, $\tilde{p}$ is the filtered pressure, ρ is the density, ν is the molecular kinematic viscosity and $\boldsymbol{\tau}^{\mathrm{sgs}}$ is the sub-grid scale stress tensor, which is modeled as follows

$$\boldsymbol{\tau}^{\mathrm{sgs}}=-2\nu_{\mathrm{sgs}}\tilde{\boldsymbol{S}} \tag{3}$$

where ν_{sgs} is the sub-grid scale eddy viscosity, $\tilde{\boldsymbol{S}}=1/2(\nabla\tilde{\boldsymbol{u}}+\nabla\tilde{\boldsymbol{u}}^{\mathrm{T}})$ is the resolved strain-rate tensor. The wall-adapting local eddy-viscosity (WALE) model[16] is adopted to calculate ν_{sgs}, which is defined as follows:

$$\nu_{\mathrm{sgs}}=(C_w\Delta)^2\frac{(S_{ij}^dS_{ij}^d)^{3/2}}{(\tilde{S}_{ij}\tilde{S}_{ij})^{5/2}+(S_{ij}^dS_{ij}^d)^{5/4}} \tag{4}$$

$$S_{ij}^d=\frac{1}{2}\left(\frac{\partial\tilde{u}_i}{\partial x_k}\frac{\partial\tilde{u}_k}{\partial x_j}+\frac{\partial\tilde{u}_j}{\partial x_k}\frac{\partial\tilde{u}_k}{\partial x_i}\right)-\frac{1}{3}\delta_{ij}\frac{\partial\tilde{u}_k}{\partial x_l}\frac{\partial\tilde{u}_l}{\partial x_k} \tag{5}$$

where C_w is the model coefficient set to 0.325 in the following simulations, $\Delta=V_C^{1/3}$ is the filter width taken as the cube-root cell volume, S_{ij}^d is the traceless symmetric part of the square of the filtered velocity gradient tensor and δ_{ij} is the Kronecker delta.

1.2 *Wall-stress modelling*

To reduce the mesh resolution in the boundary layer, WMLES is used for high Reynolds number turbulent flows in this study. In WMLES, the local wall shear stress is calculated by the wall stress model instead of using the wall-normal velocity gradient directly. To correctly predict the wall shear stress, various wall-stress models have been developed.

In the present study, the wall-stress models are derived based on the thin boundary layer equations (TBLE), which are as follows:

$$\frac{\partial}{\partial y}\left[(\nu+\nu_t)\frac{\partial\tilde{u}_i}{\partial y}\right]=S_i \tag{6}$$

$$S_i=\frac{\partial\tilde{u}_i}{\partial t}+\frac{\partial\tilde{u}_i\tilde{u}_j}{\partial x_j}+\frac{1}{\rho}\frac{\partial\tilde{p}}{\partial x_i} \tag{7}$$

where $i=1,3$ represents the wall-parallel directions, ν_t is the eddy viscosity. Among them, the relevant terms on velocity $\tilde{\boldsymbol{u}}$ and pressure $\tilde{p}$ are sampled from the cell center at a user-defined sampling distance h from the wall. Then, the wall shear stress is calculated by the wall stress model and enforced at the corresponding boundary face center. The detailed procedure can refer to Mukha et al.[11].

In the following simulations, we focus on the performance of two wall-stress models. When the source term S_i on the RHS of Eq. (6) is neglected, this simplification corresponds to the equilibrium wall model (referred to as EWSM), which are ordinary differential equations in mathematical form. When the source term only retains the pressure gradient term, i.e., $S_i=(1/\rho)(\partial\tilde{p}/\partial x_i)$, this assumption corresponds to the non-equilibrium wall model (referred to as NEWSM). Since the pressure gradient term is explicitly treated in the current implementation (S_i becomes a constant), the NEWSM remains in the form of ordinary differential equations, which has advantages in computational efficiency.

1.3 *Vortex identification methods*

In the present study, the third generation of vortex identification method Liutex proposed by Liu[17-20] is used to analyze the vortical structures. By further decomposing the vorticity vector, the extracted rigid rotation part is defined as the Liutex vector. The Liutex vector can describe the local rotational axis and rotational strength, whose explicit formula[21] can be written as

$$\boldsymbol{R}=R\boldsymbol{r}=\left[\boldsymbol{\omega}\cdot\boldsymbol{r}-\sqrt{(\boldsymbol{\omega}\cdot\boldsymbol{r})^2-4\lambda_{ci}^2}\right]\boldsymbol{r} \tag{8}$$

where R is the magnitude of Liutex vector, $\boldsymbol{r}$ is the normalized real eigenvector of the velocity gradient tensor, i.e., the Liutex direction vector, $\boldsymbol{\omega}$ is the vorticity vector and λ_{ci} is the imaginary part of the complex eigenvalue.

On this basis, the modified normalized Liutex-Omega method[22-23] ($\tilde{\Omega}_R$), combing the ideas of Liutex and Omega[24] (Ω) methods, is also adopted to capture both strong and weak vortices simultaneously in the wake, whose expression is as follows:

$$\tilde{\Omega}_R=\frac{\beta^2}{\beta^2+\alpha^2+\lambda_{cr}^2+1/2\lambda_r^2+\varepsilon} \tag{9}$$

$$\alpha=\frac{1}{2}\sqrt{(\boldsymbol{\omega}\cdot\boldsymbol{r})^2-4\lambda_{ci}^2} \tag{10}$$

$$\beta=\frac{1}{2}\boldsymbol{\omega}\cdot\boldsymbol{r} \tag{11}$$

where α and β are the components of the strain rate and vorticity tensors on the plane perpendicular to the local rotational axis, respectively, λ_{cr} is the real part of the complex eigenvalue and $\varepsilon=b_0(\beta^2-\alpha^2)_{\max}$ is a small parameter to remove computational noises. According to a sensitive study by Zhao et al.[25], b_0 is recommended to be 10^{-6} in marine hydrodynamics.

2. Numerical setup

2.1 *Computational domain and mesh*

The DARPA SUBOFF bare model without appendages[26] is used throughout the study, as shown in Fig. 1. The hull is an axisymmetric body of revolution, which consists of a forebody, a parallel middle body, and an afterbody. The maximum diameter is D, and the overall length is $L=8.6D$. In the present study, the Reynolds number based on the overall length L is $Re=1.2\times10^7$.

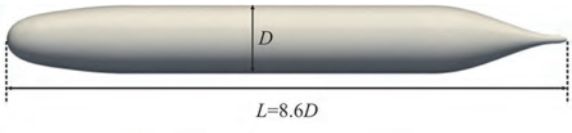

Fig. 1 Computational model

Figure 2 shows the side view of the computational domain. The origin of the reference coordinate system is at the stern of the hull. The inlet is located $10D$ upstream of the hull, and the outlet is located $30D$ downstream of the stern. To reduce the blockage effect[8], the lateral sides are located $10D$ from the origin. As a result, the rectangular computational domain is finally set to $-18.6\le x/D\le30$, $-10\le y/D\le10$ and $-10\le z/D\le10$.

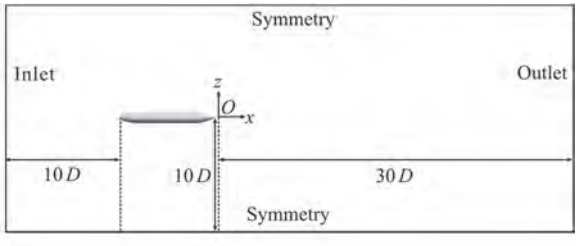

Fig. 2 Computational domain

Figure 3 shows the computational mesh, generated by the snappyHexMesh utility. The mesh is refined according to the distance to the hull, and the uniform mesh size of the highest refinement level is $7.7\times10^{-3}D$. Furthermore, the mesh refinement is extended up to $x/D=15$ with a uniform size of $1.5\times10^{-2}D$ to capture wake characteristics. For the boundary layer mesh configuration for WMLES[27-28], the overall thickness δ is first estimated using the empirical formula for a flat plate, which is as follows

$$\delta \approx 0.37\frac{x}{Re_x^{1/5}} \tag{12}$$

where x is the distance downstream from the nose of the hull, Re_x is the Reynolds number based on x. Then, the overall thickness δ is further corrected by the solution of the steady RANS simulation, where the boundary layer is determined by the criterion of 99% of the free-stream velocity. In the present study, the δ at the end of the middle parallel body is about $0.08D$. On this basis, 30 prism layers are added to the hull surface within δ, as shown in Fig. 3(c). The height of the wall-adjacent layer is $\Delta y_w = 1/50\delta$, and the expansion ratio is set to 1.03. For wall-parallel directions, the boundary layer mesh has a uniform size of $\Delta x = \Delta z = 1/10\delta$, and the maximum aspect ratio is about 5. As a consequence, the computational mesh finally consists of 2.2×10^7 cells.

2.2 *Numerical schemes*

For the LES simulations, the temporal term is discretized with the second-order implicit backward scheme. For the spatial discretization, the advection term is discretized using the second-order linear-upwind stabilised transport (LUST) scheme[29], which blends the linear scheme (75%) and the linearUpwind scheme (25%). In addition, both the gradient term $(\nabla\cdot)$ and the laplacian term $(\nabla^2\cdot)$ are discretized with the second-order linear scheme. As for the RANS simulations, the advection terms of the momentum equation and the turbulence transport equations are discretized using the second-order linearUpwind scheme. Others are consistent with the LES simulations.

For the LES simulations, the PISO algorithm[30] is used to handle the pressure-velocity coupling. The momentum equation is solved using a preconditioned bi-conjugate gradient (PBiCGStab) solver with a diagonal-based incomplete LU (DILU) preconditioner, and the tolerance is set to 10^{-7}. As for the pressure Poisson equation, it is solved using a preconditioned conjugate gradient (PCG) solver with a diagonal incomplete-Cholesky (DIC) preconditioner, and the tolerance is also set to 10^{-7}. Instead, for the RANS simulations, the SIMPLE algorithm[31] is used. Besides, the turbulence transport equations are solved using an iterative solver with a symmetric Gauss-Seidel smoother, and the tolerance is set to 10^{-6}. The convergence criterions for all variables are set to 10^{-5}.

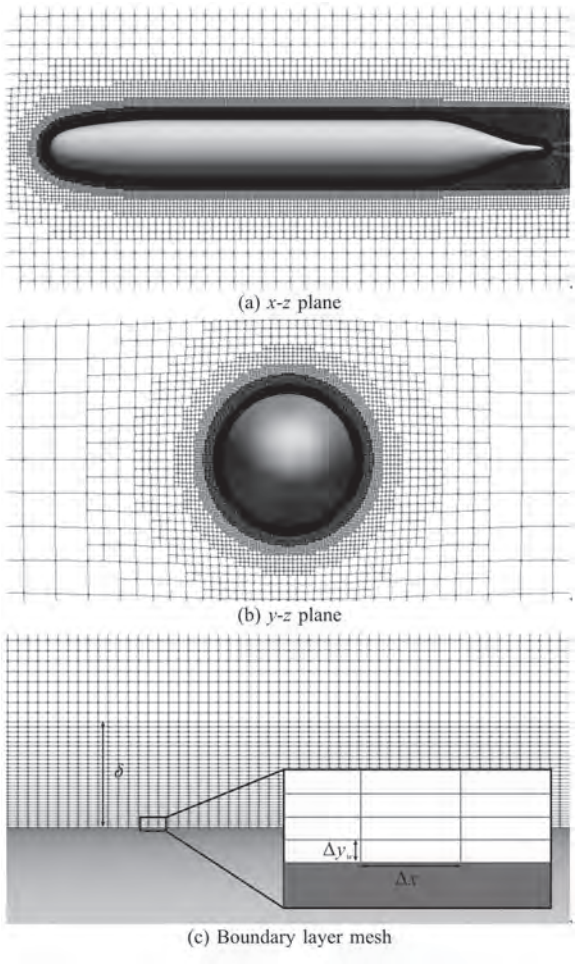

Fig. 3 Computational mesh

2.3 *Initial and boundary conditions*

The uniform inflow $(U_\infty,0,0)$ is set at the inlet, where U_∞ is the free-stream velocity. The Neumann boundary condition of zero gradient is applied to the outlet, and the symmetry boundary condition is used elsewhere. The converged solution of the steady RANS simulation (k-ω SST model) on the same mesh configuration is used as the initial conditions, including pressure and velocity.

The nondimensional time step $\Delta t^* = \Delta t U_\infty / L$ is set to 3×10^{-5}, satisfying that the maximum Courant-Friedrichs-Lewy number is less than 0.2. The statistical analysis is performed after the far wake is fully developed at about $t^* = tU_\infty / L = 2.5$.

3. Results and discussion

3.1 *Effects of wall stress model and sampling distance*

To investigate the effects of the wall shear model and sampling distance h, six test cases are adopted in the present study, as listed in Table 1. Here, for convenience, h is defined as the n^{th} consecutive off-wall cell, i.e., sampled from the n^{th} cell center. In this section, we mainly focus on the distribution of the pressure coefficient C_p and the skin-friction coefficient C_f, which are expressed as follows:

$$C_p = \frac{p - p_\infty}{1/2\rho U_\infty^2} \tag{13}$$

$$C_f = \frac{\tau_w}{1/2\rho U_\infty^2} \tag{14}$$

where p_∞ is the free-stream pressure, τ_w is the wall shear stress.

Table 1 Test cases

Case	Model	h
A	EWSM	1
B	EWSM	2
C	EWSM	3
D	NEWSM	1
E	NEWSM	2
F	NEWSM	3

Figure 4 first compares the distribution of the time-averaged pressure coefficient on the hull using the EWSM and the NEWSM. Here, h is set to 3 in both cases for consistency. The experimental data are taken from the measurements of Huang et al.[1] at $Re = 1.2\times10^7$. It can be clearly observed that the numerical results of both models agree well with the experiments, except for small oscillations near the nose of the hull. Figure 5 shows the comparison of different sampling distances, in which the NEWSM is used. In general, the numerical results of different h are almost identical. However, as h increases, the numerical simulation gives better prediction in the stern region of the hull. On the other hand, the small oscillations near the nose of the hull gradually improve as h decreases.

Figure 6 shows the comparison of the time-averaged skin-friction coefficient on the hull using the EWSM and the NEWSM, where h is set to 3. Since τ_w in WMLES is computed by the wall stress model, the accuracy of the wall stress model can be largely inferred from the skin-friction coefficient. Through comparison, it can be found that the EWSM and the NEWSM give similar results in the middle parallel region, which are in good agreement with the experimental measurements. This is due to the equilibrium state of the turbulent boundary layer in this region, as reported in the WRLES by Posa and Balaras[7]. However, the NEWSM performs better near the nose and stern where the pressure gradient exists. This improvement can be attributed to the inclusion of the pressure gradient term in the NEWSM. On this basis, Fig. 7 further compares the results of different sampling distances, and the NEWSM is adopted. In contrast to the pressure coefficient, the sampling distance has a significant effect on the skin-friction coefficient, especially in the middle parallel region. As the sampling point gradually gets closer to the hull surface, the numerical results are increasingly underestimated, and can even be reduced by 40% in the middle parallel region. The numerical result of $h = 3$ is in excellent agreement with the experiments, and the corresponding sampling point is $1/20\delta$ away from the hull surface. Nevertheless, it should be noted that more simulations are still required to find out the variation of h under different conditions in the future.

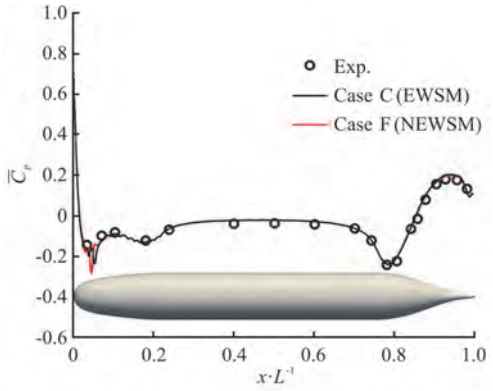

Fig. 4 (Color online) Comparison of time-averaged pressure coefficient on the hull using different wall stress models

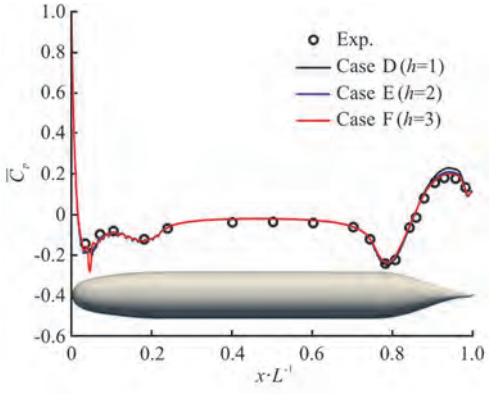

Fig. 5 (Color online) Comparison of time-averaged pressure coefficient on the hull using different sampling distances

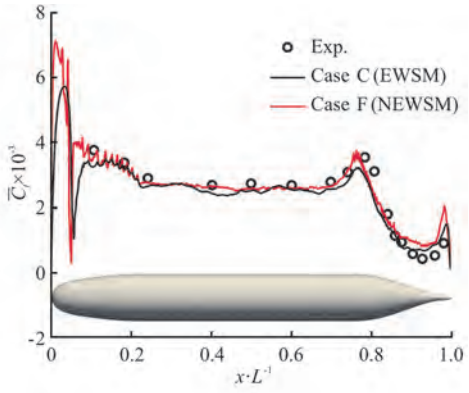

Fig. 6 (Color online) Comparison of time-averaged skin-friction coefficient on the hull using different wall stress models

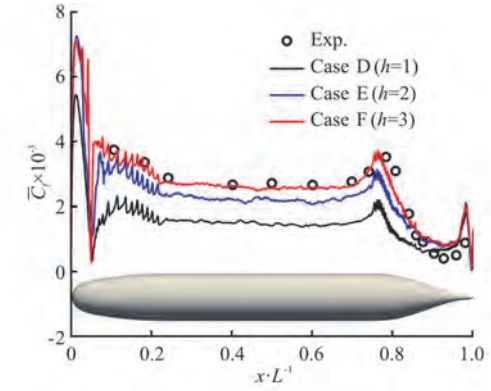

Fig. 7 (Color online) Comparison of time-averaged skin-friction coefficient on the hull using different sampling distances

Since the drag force is closely related to the skin-friction coefficient, the drag coefficient is further compared in Table 2, and its expression is as follows

$$C_D = \frac{F}{1/2\rho U_\infty^2 S} \tag{15}$$

where F is the drag force and $S = 0.25\pi D^2$ is the streamwise projected area. Here, the experimental data is taken from the towing tank tests of Liu and Huang[2]. Similarly, it can be observed that the predictions of the NEWSM are closer to the experimental measurements at all sampling distances. In addition, using the same wall stress model, the relative error becomes smaller as the sampling point is away from the hull surface. As a result, the numerical result of case F can achieve a relative error of about 5%, which is acceptable for engineering problems.

Figure 8 compares the time-averaged pressure coefficient profiles in the stern region, which are $x/L = -0.096$, -0.022. Here, r_0 is the local maximum radius, R is the maximum radius. Since the differences between each case are not significant, only the results of case F are shown here. Overall, the numerical results are in good agreement with the experimental measurements. A slight overprediction can be found at $x/L = -0.096$, which may be attributed to the earlier flow separation in the experiments.

Table 2 Comparison of time-averaged drag coefficient

Case	CFD	Exp.[2]	Error/%
A	0.047	0.093	49.5
B	0.070	0.093	24.5
C	0.084	0.093	9.96
D	0.048	0.093	48.6
E	0.074	0.093	20.9
F	0.088	0.093	5.21

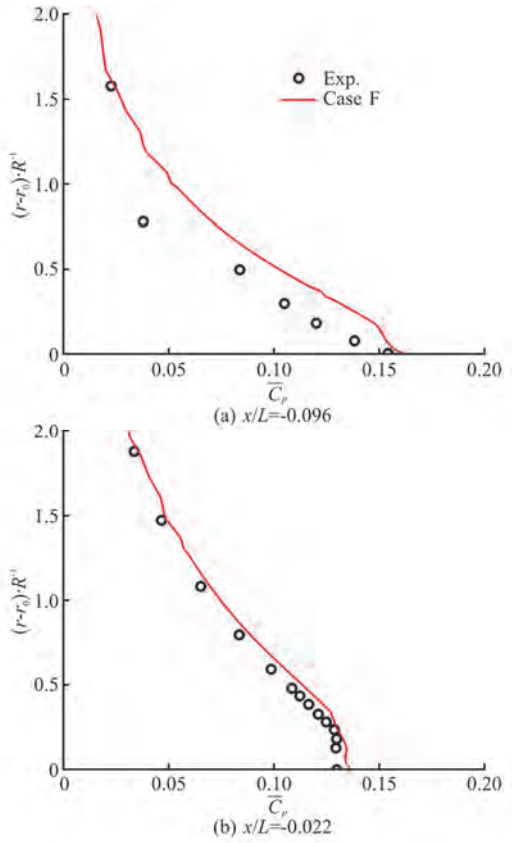

Fig. 8 (Color online) Comparison of time-averaged pressure coefficient profiles in the stern region

Correspondingly, Figs. 9 and 10 further compares the time-averaged normalized streamwise and radial velocity profiles in the stern region. Here, U_x is the streamwise velocity and U_r is the radial velocity. The numerical results agree well with the experiments. In addition, the thickening of the boundary layer can also be inferred from the streamwise velocity profiles.

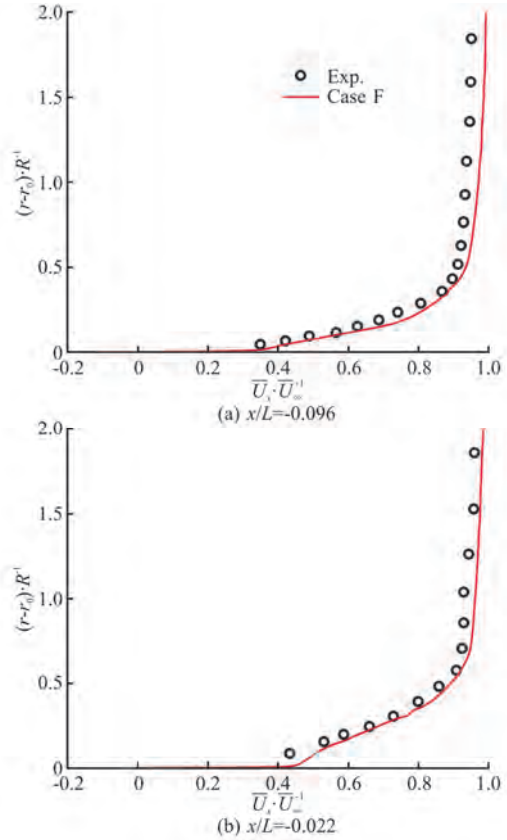

Fig. 9 (Color online) Comparison of time-averaged normalized streamwise velocity profiles in the stern region

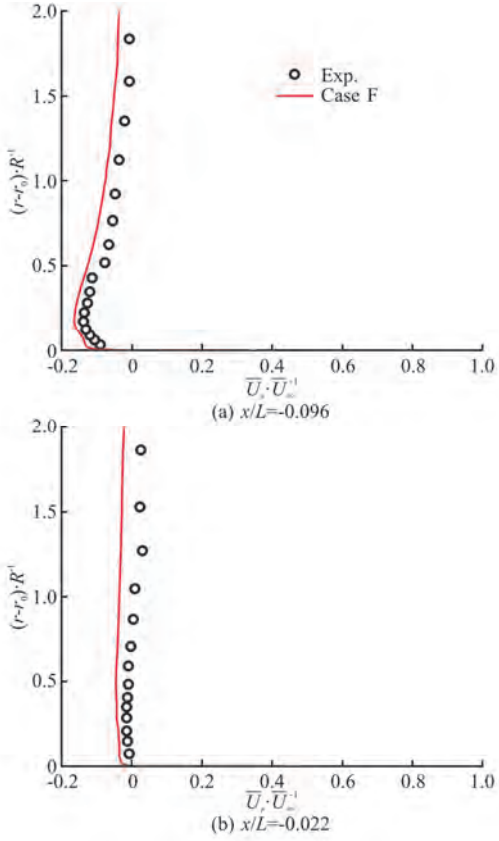

Fig. 10 (Color online) Comparison of time-averaged normalized radial velocity profiles in the stern region

3.2 *Flow field analysis*

To gain insight into the flow mechanism, the flow field is visualized and analyzed in this section. Figure 11 shows the instantaneous flow field in the symmetry plane $y/D=0$, including the streamwise velocity, pressure coefficient, turbulent kinetic energy and Liutex magnitude. Figure 11(a) shows that the flow separates on the stern and forms the wake, which is also evident in the far field. A high-pressure region can be identified near the front stagnation point, as shown in Fig. 11(b). For the middle parallel region, the pressure remains almost constant, i.e., zero pressure gradient, which can also be observed in Figs. 4, 5. When approaching the stern, the pressure decreases due to flow separation. In addition, pressure fluctuations persist even in the far wake, which is correlated with the noise generation. For the turbulent kinetic energy, its overall distribution is symmetric about $z/D=0$, as shown in Fig. 11(c). As the flow develops downstream, the turbulent kinetic energy gradually increases near the hull, then reaches a peak on the stern and is finally dissipated in the wake. Figure 11(d) shows the Liutex magnitude, which can reveal the overall distribution of vortical structures in the flow field. The Liutex magnitude increases downstream along the hull, indicating the development of the turbulent boundary layer. Furthermore, the Liutex magnitude suggests that the fluctuations in the flow field can be attributed to the vortical structures involved, which will be visualized later. Figure 12 shows the time-averaged square of the pressure oscillation on the hull. The transition point can be clearly identified downstream of the nose, where pressure oscillations are highest. Besides, the pressure oscillations are also evident on the forebody and stern, possibly due to the pressure gradient.

Figure 13 shows the instantaneous three-dimensional vortical structures using the iso-surface of $\tilde{\Omega}_R=0.52$ with the symmetry plane $y/D=0$ showing the Liutex magnitude. The modified Omega-Liutex method can well exclude the shearing contamination in the laminar region, which can be seen near the nose. After the transition position, the vortical structures attached to the hull grow rapidly and thicken due to the development of the turbulent boundary layer along the hull. At the same time, due to the flow separation on the stern, the wake region contains a large number of vortical structures. Furthermore, with the normalized streamwise velocity, it can be found that the flow accelerates on the stern which

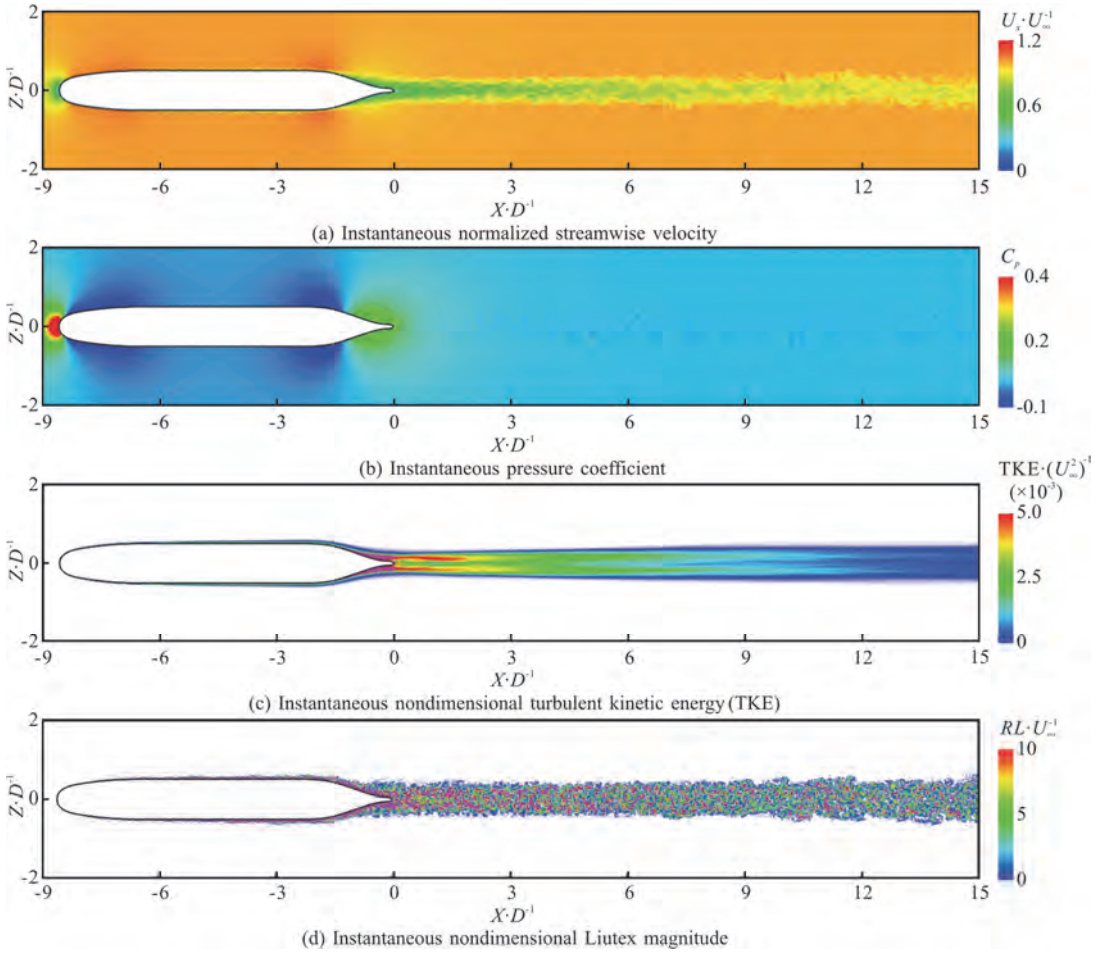

Fig. 11 (Color online) Instantaneous flow field in the symmetry plane $y/D=0$

Fig. 12 (Color online) Time-averaged square of the pressure oscillation on the hull

can be attributed to the favourable pressure gradient.

In order to better reveal the development of the turbulent boundary layer, Fig. 14 shows the magnified views of the Liutex magnitude at different locations near the hull. The black solid lines represent the hull surface. The thickening of the boundary layer along the hull can be clearly observed in the longitudinal plane, as shown in Fig. 14(a). Furthermore, Figs. 14(b)-14(d) shows the radial distribution of three transverse planes, two of which are in the middle parallel region and one on the stern. After the transition occurs, the turbulent boundary layer in the middle parallel region gradually thickens downstream, as indicated by the occupied area in the radial direction. On the stern, more vortical structures are generated near the hull surface induced by nearby flow separation.

To further investigate the development of the wake, Fig. 15 shows the Liutex magnitude at five streamwise locations in the wake, which are $x/D=3$, 6, 9, 12 and 15. The black dashed lines illustrate the maximum diameter of the hull. In the near wake, the distribution is almost axisymmetric and concentrated near the center, as shown in Figs. 15(a), 15(b). As it moves downstream, Figs. 15(d), 15(e) shows that the wake tends to expand radially, eventually exceeding the maximum diameter of the hull.

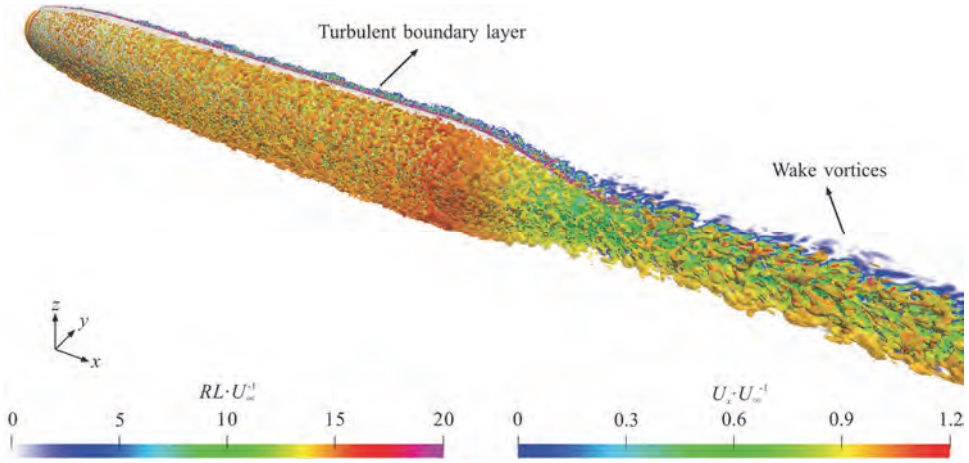

Fig. 13 (Color online) Instantaneous vortical structures using the iso-surface of $\tilde{\Omega}_R = 0.52$ with the symmetry plane $y/D = 0$ showing the Liutex magnitude

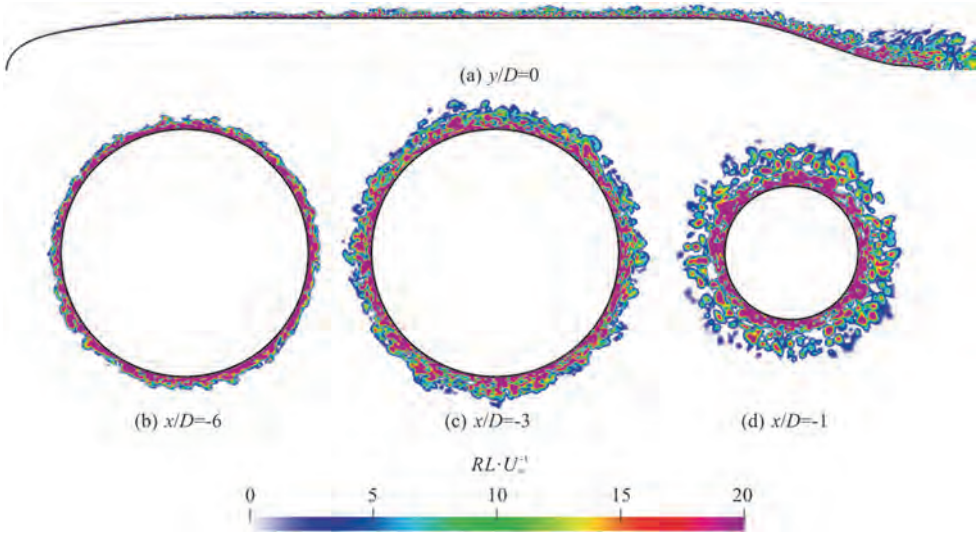

Fig. 14 (Color online) Instantaneous Liutex magnitude at different locations near the hull

4. Conclusions

In this paper, the WMLES is used to carried out numerical simulations of the flow around an axisymmetric body of revolution (DARPA SUBOFF bare model) at $Re = 1.2\times10^7$. Through the comparison with experimental measurements, the effects of the wall stress model and sampling distance are systematically investigated. On this basis, the flow field is analyzed in detail, with emphasis on the developments of the turbulent boundary layer and the wake using the Liutex method. The main conclusions are as follows:

In general, the non-equilibrium wall stress model predicts better than the equilibrium model in terms of pressure coefficient distribution, skin-friction coefficient distribution, and drag coefficient. Nevertheless, both models give similar results in the middle parallel region, i.e., zero pressure gradient region. Moreover, the numerical results are sensitive to the sampling distance. An appropriate value of $h = 3$ can achieve good agreements with the experiments, which corresponds to a sampling distance of $1/20\delta$.

Visualization of the flow field reveals the flow characteristics involved, such as the flow transition near the nose and the flow separation on the stern. Furthermore, the developments of the turbulent boundary layer and the wake can be clearly observed using the Liutex method. After the transition occurs, the turbulent boundary layer gradually thickens downstream along the hull surface. On the other hand, the near wake is axisymmetric and more concentrated near the center. However, the wake gradually expands radially downstream.

In the near future, we plan to focus on the performance of WMLES in predicting the fluctuation quan-

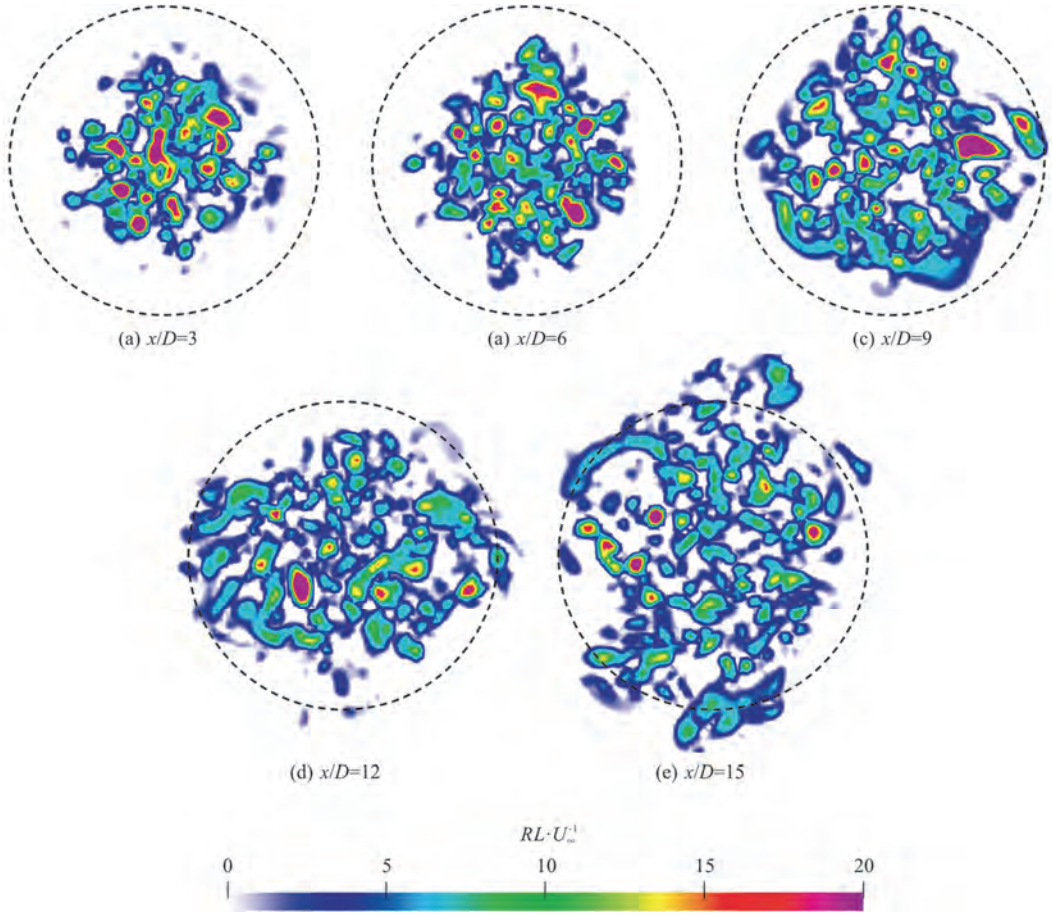

Fig. 15 (Color online) Instantaneous Liutex magnitude at different streamwise locations in the wake

tities of the flow field, serving for underwater noise prediction. At the same time, we will improve the current wall modeling strategy, such as achieving the zonal modeling in particular regions.

Acknowledgement

(This research received other funding agency in the public, commercial, or not-for-profit sectors.)

Compliance with ethical standards

Conflict of interest: The authors declare that they have no conflict of interest. De-cheng Wan is an editorial board member for the Journal of Hydrodynamics and was not involved in the editorial review, or the decision to publish this article. All authors declare that there are no other competing interests.

Ethical approval: This article does not contain any studies with human participants or animals performed by any of the authors.

Informed consent: Informed consent was obtained from all individual participants included in the study.

References

[1] Huang T., Liu H. L., Groves N. et al. Measurements of flows over an axisymmetric body with various appendages in a wind tunnel: The DARPA SUBOFF experimental pro- gram [C]. *Proceedings of the 19th Symposium on Naval Hydrodynamics*, Seoul, Korea, 1992.

[2] Liu H. L., Huang T. T. Summary of DARPA SUBOFF experimental program data [R]. Bethesda, USA: Naval Surface Warfare Center, 1998.

[3] Jiménez J. M., Hultmark M., Smits A. J. The intermediate wake of a body of revolution at high Reynolds numbers [J]. *Journal of Fluid Mechanics*, 2010, 659: 516-539.

[4] Toxopeus S. Viscous-flow calculations for bare hull DARPA SUBOFF submarine at incidence [J]. *International Shipbuilding Progress*, 2008, 55(3): 227-251.

[5] Chase N., Carrica P. M. Submarine propeller computations and application to self-propulsion of DARPA Suboff [J]. *Ocean Engineering*, 2013, 60: 68-80.

[6] Liu Y., Zhou Z., Zhu L. et al. Numerical investigation of flows around an axisymmetric body of revolution by using Reynolds-stress model based hybrid Reynolds-averaged Navier-Stokes/large eddy simulation [J]. *Physics of Fluids*, 2021, 33(8): 085115.

[7] Posa A., Balaras E. A numerical investigation of the wake of an axisymmetric body with appendages [J]. *Journal of*

Fluid Mechanics, 2016, 792: 470-498.
[8] Kumar P., Mahesh K. Large-eddy simulation of flow over an axisymmetric body of revolution [J]. *Journal of Fluid Mechanics*, 2018, 853: 537-563.
[9] Piomelli U., Balaras E. Wall-layer models for large-eddy simulations [J]. *Annual Review of Fluid Mechanics*, 2002, 34(1): 349-374.
[10] Bose S. T., Park G. I. Wall-modeled large-eddy simulation for complex turbulent flows [J]. *Annual Review of Fluid Mechanics*, 2018, 50: 535-561.
[11] Mukha T., Rezaeiravesh S., Liefvendahl M. A library for wall-modelled large-eddy simulation based on OpenFOAM technology [J]. *Computer Physics Communications*, 2019, 239: 204-224.
[12] Posa A., Balaras E. A numerical investigation about the effects of Reynolds number on the flow around an appended axisymmetric body of revolution [J]. *Journal of Fluid Mechanics*, 2020, 884: A41.
[13] Shi B., Yang X., Jin G. et al. Wall-modeling for large-eddy simulation of flows around an axisymmetric body using the diffuse-interface immersed boundary method [J]. *Applied Mathematics and Mechanics (English Edition)*, 2019, 40(3): 305-320.
[14] Zhou Z., Xu Z., Wang S. et al. Wall-modeled large-eddy simulation of noise generated by turbulence around an appended axisymmetric body of revolution [J]. *Journal of Hydrodynamics*, 2022, 34(4): 533–554.
[15] Zhou D., Wang K., Wang M. Large-eddy simulation of an axisymmetric boundary layer on a body of revolution [C]. *Proceeding of AIAA Aviation Forum*, virtual event, 2022.
[16] Nicoud F., Ducros F. Subgrid-scale stress modelling based on the square of the velocity gradient tensor [J]. *Flow, Turbulence and Combustion*, 1999, 62(3): 183-200.
[17] Liu C., Gao Y., Tian S. et al. Rortex-A new vortex vector definition and vorticity tensor and vector decompositions [J]. *Physics of Fluids*, 2018, 30(3): 035103.
[18] Gao Y., Liu C. Rortex and comparison with eigenvalue-based vortex identification criteria [J]. *Physics of Fluids*, 2018, 30(8): 085107.
[19] Liu C., Yu Y. Mathematical foundation of Liutex theory [J]. *Journal of Hydrodynamics*, 2022, 34(6): 981-993.
[20] Liu C., Yu Y., Gao Y. S. Liutex based new fluid kinematics [J]. *Journal of Hydrodynamics*, 2022, 34(3): 355-371.
[21] Wang Y. Q., Gao Y. S., Liu J. M. et al. Explicit formula for the Liutex vector and physical meaning of vorticity based on the Liutex-Shear decomposition [J]. *Journal of Hydrodynamics*, 2019, 31(3): 464-474.
[22] Dong X., Gao Y., Liu C. New normalized Rortex/vortex identification method [J]. *Physics of Fluids*, 2019, 31(1): 011701.
[23] Liu J., Liu C. Modified normalized Rortex/vortex identification method [J]. *Physics of Fluids*, 2019, 31(6): 061704.
[24] Liu C., Wang Y. Q., Yang Y. et al. New omega vortex identification method [J]. *Science China Physics, Mechanics and Astronomy*, 2016, 59(8): 684711.
[25] Zhao W. W., Wang J. H., Wan D. C. Vortex identification methods in marine hydrodynamics [J]. *Journal of Hydrodynamics*, 2020, 32(2): 286-295.
[26] Groves N. C., Huang T. T., Chang M. S. Geometric characteristics of DARPA (Defense Advanced Research Projects Agency) SUBOFF models (DTRC model numbers 5470 and 5471) [R]. Bethesda, USA: David Taylor Research Center, 1989.
[27] Larsson J., Kawai S., Bodart J. et al. Large eddy simulation with modeled wall-stress: Recent progress and future directions [J]. *Mechanical Engineering Reviews*, 2016, 3(1): 00418.
[28] Menter F. R. Best practice: Scale-resolving simulations in ANSYS CFD [R]. ANSYS Germany GmbH, 2012.
[29] Weller H. Controlling the computational modes of the arbitrarily structured C grid [J]. *Monthly Weather Review*, 2012, 140(10): 3220-3234.
[30] Issa R. I. Solution of the implicitly discretised fluid flow equations by operator-splitting [J]. *Journal of computational physics*, 1986, 62(1): 40-65.
[31] Caretto L. S., Gosman A. D., Patankar S. V. et al. Two calculation procedures for steady, three-dimensional flows with recirculation [C]. *Proceedings of the Third International Conference on Numerical Methods in Fluid Mechanics*, Paris, France, 1973, 60-68.